The 8th European Congress on Computational Methods in Applied Sciences and Engineering
ECCOMAS Congress 2022
5–-9 June 2022, Oslo, Norway

UNSTRUCTURED HIGH-ORDER SOLUTIONS OF HOVERING ROTORS WITH AND WITHOUT GROUND EFFECT

Paulo A. S. F. Silva[1], **Panagiotis Tsoutsanis**[1], **Antonis F. Antoniadis**[1] **and Karl W. Jenkins**[1]

[1] Centre for Computational Engineering sciences, Cranfield University - Cranfield MK43 0AL, United Kingdom

Key words: High-order methods, Unstructured hybrid mesh, Hovering flows, MUSCL, WENO

Abstract. This work describes the computational cost and accuracy of high-order numerical schemes on a simplified concept of multiple reference frame (MRF) technique using mixed-element unstructured grid framework widely tested for aerospace applications. The Reynolds averaged Navier-Stokes equations are approximated with up to fourth spatial order using Spalart Allmaras turbulence model on two types of reconstruction scheme: monotonic upwind scheme for conservation laws (MUSCL) and weighted non-oscillatory (WENO). The calculations were made for both out-of-ground-effect (OGE) and in-ground-effect (IGE) cases and compared with experimental data in terms of pressure distribution, tip-vortex trajectory, vorticity contours and integrated thrust and torque. The predictions were obtained for several ground distances. Our findings suggest that the resolution of the vortex path and wake breakdown were considerably improved with increased scheme order. It is noticeable how low-order scheme struggles to deal with the large amount of diffusion. This numerical nature contributes to the vortex system settle down and achieve this stable ring state structure as seen on a couple radii downstream the rotor. As the wake is transported downwards, it can be clearly seen the interaction primary and secondary structures, which stretch between the tip vortices making an S-shaped path also seen experimentally. The presence of the vortex-ring close to the rotor blade contributes to a larger induced flow and under predictions of thrust coefficient . As we increase the scheme-order, it becomes more evident how the helical system convects down and breakdown toroidal vortex into smaller scales.

1 Introduction

Accurate predicting the forces on helicopter blade aerodynamics encompass several issues that challenges most of computational fluid dynamics codes. Low-order methods (≤ 2) lacks in the robustness and efficiency addressing physics such as shock capturing and vortex dominated flow. The low numerical dissipation properties enhanced discontinuities capturing abilities make the high-orders methods most wanted o this application, but it comes with an additional computational cost.

The use of high-order schemes on block structured blocks has promoted the development of overset meshes to assess rotary wings problems. This powerful combination established this technique as standard to handle the relative motion of the blade. Chen-Long et al.[1] assessed the capability of the Overset and other methods such as sliding-mesh and moving reference frame to perform a low-order simulation of the hovering Caradonna and Tung rotor. These methods were compared in terms of velocity and pressure field and differences were pointed in terms of accuracy, mesh and convergence time. It is highlighted that sliding-mesh and moving reference frame are slightly less accurate than Overset in capturing shock waves, but they require considerable lower computational cost. Hwang et al. [2] assessed the ground effect of the S-76 hovering rotor for three blades geometries using overset unstructured mesh approach and high-order WENO reconstruction in the off-body regions. Hu et al.[3] coupled CFD with a discrete element method to investigate the dust cloud and the motion of sediment particles with the ground effect. Stokkermans et al. [4] uses high-fidelity CFD to study aerodynamic interactions between rotors of a compound helicopter. Pasquali et al.[5] presented a numerical and experimental correlation to predict the rotor aerodynamic in the presence of close ground. Recently, a research effort has been made on using this dissipative numerical techniques to understand the wake-breakdown phenomena and braid secondary vortex [6, 7]

This works discuss influence of the numerical discretization on hovering flows using an unstructured open-source CFD code: UCNS3D [8] . The governing equations are discretised using multiple reference frame velocity formulation[9], the Harten-Lax-van-Leer-Contact (HLLC) Riemann solver [10], the spatial discretisation employs the [11] MUSCL-MOGE variant limiter of Tsoutsanis [12] . The solution is advanced in time is with the block Jacobi implicit backward Euler time integration. The CFD solver labelled Unstructured Compressible Navier-Stokes 3D (UCNS3D) which is validated, assessed and evaluated across a wide range of flow conditions [13, 14, 15, 16, 17, 18, 19, 20, 21, 22, 23, 24, 25, 26, 27, 28, 29, 9, 30, 31, 8, 32, 33, 34, 35] . The solution is compared with experimental data in terms of aerodynamic performance and vortex trajectory. The cost and accuracy of each method are quantified in terms of aerodynamic forces and q-criteria are used to investigate the numerical resolution and the vortex evolution with and without the ground.

2 Numerical Framework

The unstructured, compressible, Navier-Stokes and three-dimensional open source code UCNS3D [8] is used as CFD solver this study. It solves the governing equations with several high-order spatial discretisation schemes including several MUSCL and WENO variants across a wide range of flow conditions. The Reynolds Averaged Navier-stokes (RANS) governing equations is discretised by using cell-centred finite volume method where the Spalart-Allmaras turbulence model is employed. The Monotone Upstream-centred Schemes for Conservation Laws (MUSCL) [36, 37] is used to provide 3rd order accuracy in space. The governing equations are formulated in a multiple reference frame, the Harten-Lax-van-Leer-Contact (HLLC) Riemann solver [11] with the MUSCL-MOGE variant limiter of Tsoutsanis [12] computes the inviscid fluxes. The frame of reference is defined at the solver level with no need of mesh-based interface. The velocity components are computed in absolute formulation within the appropriate flux correction according to the element frame of reference, for a more detailed description of the implementation and validation of this technique the reader must refer to [9]. The solution advances in time with the implicit backward Euler time integration with a local time-stepping strategy. The Block Jacobi relaxation method solves the linear system of equation in which the Jacobian on the non-inertial source terms are included on the lower and upper diagonalization pre-conditioning to improve the stability on high Courant-Friedricks-Lewy (CFL) numbers. The flow solver is parallelized using the ParMeTis grid partitioning and hybrid MPI/OMP paradigm for improving the computational efficiency.

Hover solutions near ground are highly unsteady and challenges the convergence of the steady-state solvers. The domain experiences a wide range of velocity field, having high values on the tip blade and near-zero quantities on the farfield. This contrast in the velocity range in addition to the strong source terms makes this set of equations numerically stiff. The use of the implicit block Jacobi iteration algorithm based on local time-stepping improves the stability of the computation with a moderate memory requirements at reasonable convergence rate [38]. In all simulations performed in this work, the steady-state solution were achieved within at least 10^5 iteration steps using CFL number of 15.

3 Results

The numerical performance of the developed framework is assessed against three distinct hovering rotorcrafts flow cases: Caradonna and Tung [39], PSP[40] and S-76 [41]. This choice was mainly based on the geometry information and measured data availability. These experimental dataset covers a great range flow regimes, Mach tip velocity and geometry complexity.

4 Caradonna and Tung

4.0.1 Pressure distribution

The two-bladed Caradonna and Tung [39] rotor tested at NASA Ames Research Center present one the most important cases for code validation. Two main aspects of the flow around the blade were measured: the surface pressure distribution by pressure tubes in five radial sections and the tip vortex strength and trajectory captured by hot-wire probes mounted underneath the rotor. The case with a blade tip Mach number of $M_{tip} = 0.89$ and pitch angles of $\theta_c = 8^\circ$ is reproduced here.

After a consistent refinement on the blade and wake, the mesh with 15.4×10^6 elements is selected to present the results. Fig.1 shows the effect of the scheme-order on capturing the pressure coefficient at the tip blade, $r/R = 0.96$. The flow experiences a shock at $x/c \approx 0.25$ and capturing it challenges most of the numerical schemes. The low-order predictions struggles to deal with the sharp pressure drop and its recovery as it presents small spurious oscillations at $0.35 < x/c < 0.6$. Due to the low dissipative nature, the higher-order solutions are more stable at the shock and are in good agreement with experimental data.

4.0.2 Vortex Trajectory

Figure 2 shows the computed tip vortex trajectories compared with the experiment hot-wires measurements [39] and prescribed wake models [42]. In terms of vortex radial contraction (r/R), Fig. 2 (a), the numerical solution agrees well with the experimental data up to the fist blade passage (180°. After this point, it looses its accuracy. This deviation may be associated the effect of the rotor hub which is neglected in the present computational model. The fourth-order scheme performs slightly better than others, however the effect on the numerical scheme on the

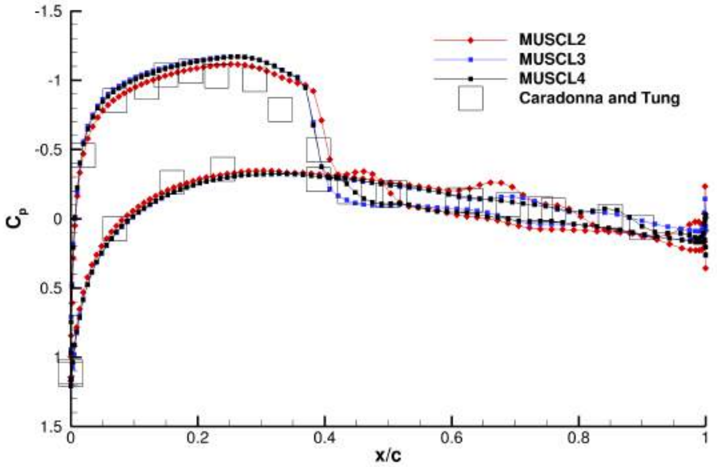

Figure 1: Pressure Coefficient at $r/R = 0.97$ for all orders.

radial contraction is negligible. Overall, the computed solutions of the vortex contraction agrees with the prescribed Kocurek wake models [42]. In terms of vertical displacement (Z/R) of the tip vortex, Fig. 2 (b) shows that the CFD results accurately predict the slow convection of the vortices up to a full cycle.

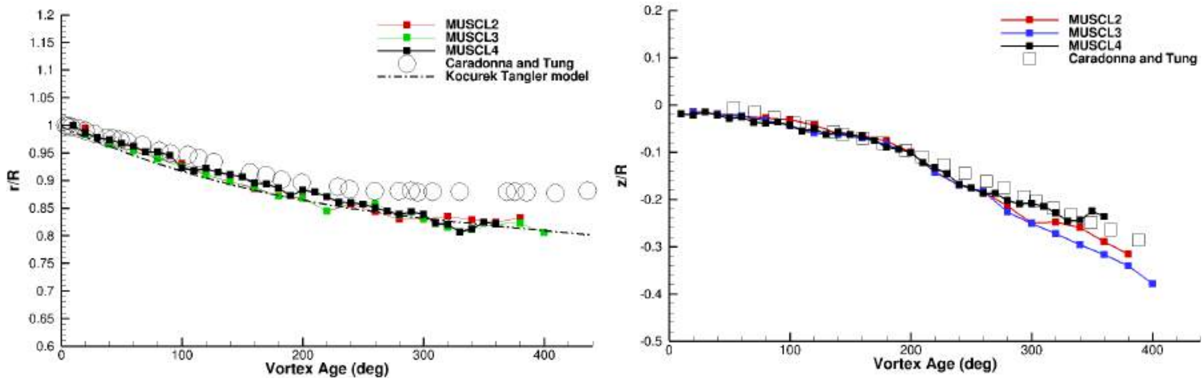

Figure 2: Vortex age and trajectory of computed solutions in terms of vortex radial contraction (a) and downwash rate (b) against azimuth angle compared with experiment

Figure 3 shows the iso q-criteria surfaces colored by the vorticity magnitude for all simulations. The advantage of increasing the numerical order on capturing the vortex resolution is clear. The low-order scheme struggles to deal with the large amount of diffusion and the vortex system settle down achieving ring state structure as seen on the couple radii downstream the rotor. On higher-order calculations, the ring vortex is pushed further down. As we increase the scheme-order, it becomes more evident how the helical system convects down and breakdown toroidal vortex into smaller scales. It can be seen that the induced vortices once present on low-order scheme strain into vortex tube as the numerical dissipation decreases. This behaviour is also seen in similar works regarding the influence of the local mesh refinement on the vortex wake breakdown [7]. This interaction primary and secondary structures, which stretch between the tip vortices making an S-shaped path also seen experimentally [43]. . The ground effect on the isolated

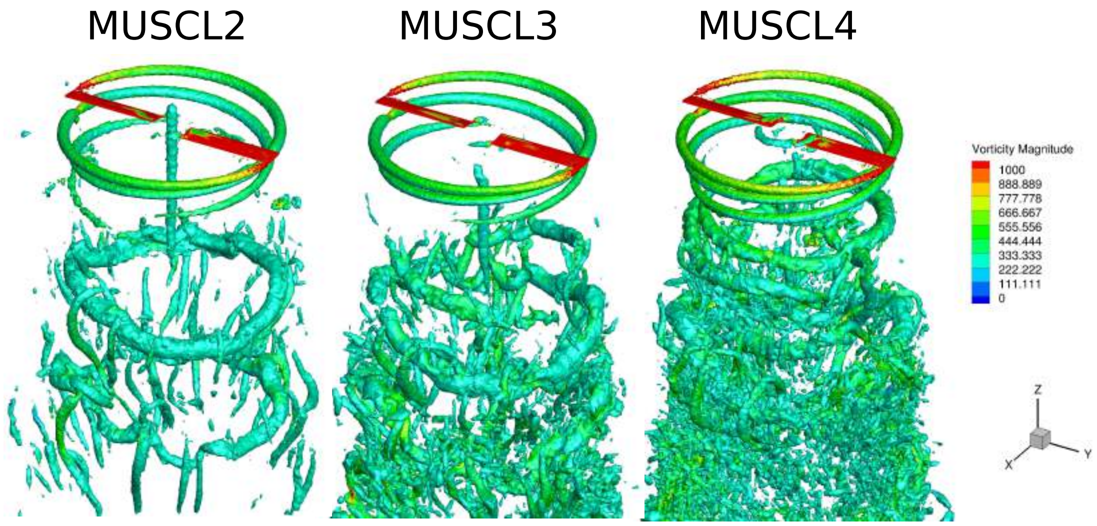

Figure 3: Iso-vortex surfaces colored by vorticity magnitude contours comparing the effect of order resolution of vortex wake.

rotor Caradonna and Tung was assessed for three different distances $Z/R = 0.5, 1.0, 3.0$. Fig. 4 shows the isosurface of q-criteria for all in-ground simulations. In comparison with the out of ground simulations, a stronger upwash flow is experienced on the presence of the ground. It is noticeable the ground vortex expanding radially due to the influence of the incoming flow. The dissipative nature of the higher-order schemes provide more detail about vortex structures due to the proximity to the ground and its breakdown in smaller scales. Capturing these structures are challenging for unstructured meshes. Fig. 5 shows the effect of the ground on the tip vortex trajectory. The computations of the fourth-order accurate MUSCL are presented for radial and vertical positions for a range of the azimuth angle from zero to 400 degrees. For the radial contraction, Fig 5 (a), the prediction whithout the ground effect agrees well with prescribed wake-models of Kocurek-Tangler [42]. The grounds shows negligible influence on effect up to the first blade passage at 180 degrees. Then, the slope for IGE simulations changes significantly, especially for $Z/R = 0.5$, as the tip vortices expands as it approaches the ground. In terms of tip vortices vertical displacement (z/R), seen in Fig 5 (b), apart from small fluctuations for $Z/R = 0.5$ no differences was found with the ground effect. Until the first passage, the tip vortex moves at slow pace. After this point, it moves a marginally faster rate. The size of tip vortex core is measured based for the same vorticity magnitude level for both IGE and OGE simulations. Fig. 5 (c) shows the growth of the vortex core radius normalized by the chord (c= 0.1905m). The tip vortex grows rapidly up to 30 deg. Then, it remains about the same size until the blade passage and it suddenly contracts due to the Blade Vortex Interaction (BVI) as shown in the detail. Overall, the ground distance shows no correlation with the vortex core size,

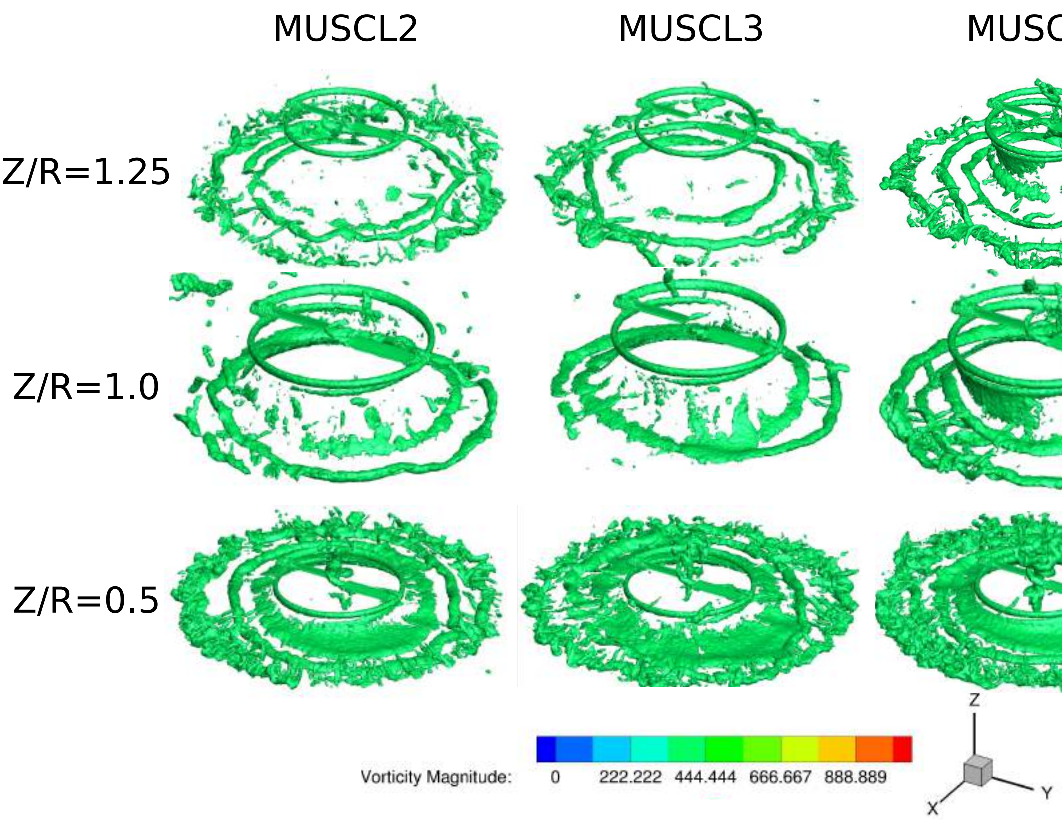

Figure 4: Iso-vorticity surface at different ground distance on Caradonna rotor comparing the effect of the spatial accuracy order on the wake vortex.

but with the shape due stronger induced flow, especially after 240 degrees age at $Z/R = 0.5$.

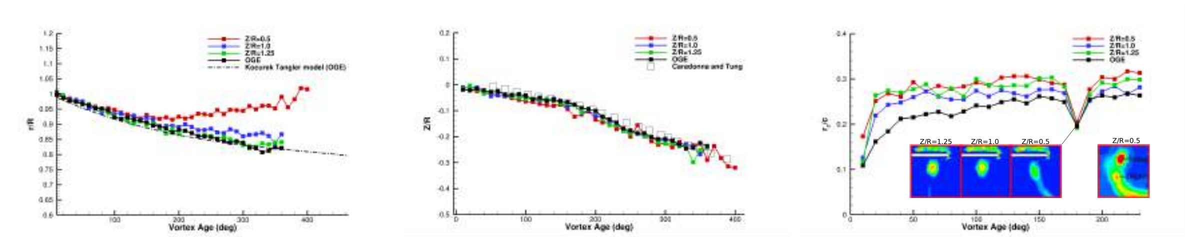

Figure 5: Vortex age and trajectory of computed solutions in terms of vortex radial contraction (a), downwash rate (b) and against azimuth angle compared with experiment (c) size of the vortex core versus wake age (in degrees) for the Caradonna and tung rotor

4.1 PSP Rotor

4.1.1 Computational cost and Integrated Load accuracy

The flow over the PSP (Pressure Sensitive Paint) rotor is simulated, Watkins et al. [40] carried out extensive experimental activities on this configuration. The main specifications of the blade are summarised in the table 1. Further details concerning the aerofoil coordinates and blade radial twist and chord distribution are presented by Noonan[44] and Watkins et al. [40], respectively.

To evaluate the cost of each method the computational domain was reduced to a quarter of a cylinder by using the rotational periodicity. A grid refinement strategy is conducted, the grids are generated based on the number of points on the aerofoil section, blade span and regions of interest, details on the grids are tabulated in Tab. 2.

Table 1: Specifications and operating conditions of the PSP flow [40]

Parameter	Value
Number of blades	4
Radius (R)	s 1.69m
Blade chord (c)	0.14m
Rotor solidity	0.1033
linear twist angle	$-14°$
Pitch angle	$8.68°, 10°$ and $12°$
M_{tip}	0.585
ρ_∞	1.2168 kg/m^3
T_∞	290° K
p_∞	101325 Pa

Table 2: Grid specifications of the PSP rotor simulations.

Mesh	Blade Elements				Volume Elements [10^6]				
	Upper	Lower	Span	Total [10^3]	Hexa	Tetra	Pyra	Prism	Total
Coarse	30	30	397	45	1.7	0.66	0.22	0.037	**2.64**
Medium	50	50	880	102	5.4	1.5	0.057	0.066	**7.6**
Fine	100	100	1080	223	10.6	3.5	1.1	0.023	**15.2**

The convergence decay of each scheme on the medium mesh is shown in figure 6 in terms of l^2 norms for the mass conservation equation per accumulated iteration number. Both spatial schemes have similar convergence rate, but WENO shows smoother trend. The Fourth-order MUSCL exhibits fluctuations which may be attributed to the combination of low dissipation and inefficiency of slope-limiters to dismiss spurious oscillations. Other works seems to overcome this issue by introducing an artificial dissipation technique [45].

One of the main properties to assess the aerodynamic performance of hovering rotor is the Figure of Merit ($FoM = C_t^{3/2}/\sqrt{2}C_Q$, where C_Q is the power coefficient and C_t the thrust

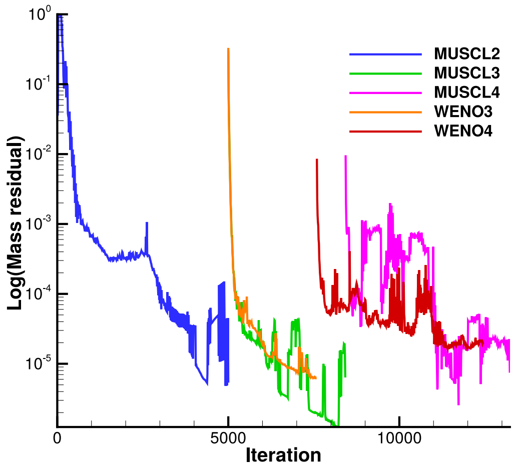

Figure 6: Continuity residuals per accumulated iteration for the flow around the PSP rotor. Solutions are shown for all numerical schemes on the medium mesh.

coefficient). This dimensionless parameter evaluates the amount of generated thrust for given power as the ratio of the ideal power required to hover over the actual power required. Figure 7 shows a comparison between all grids and schemes with the measured data[46] and other numerical works[47, 48, 49]. The case with pitch angle equal to 12° is used as the selecting point for grid and numerical schemes order, as it corresponds to the one of the highest thrust tested and challenging for CFD methods. Lower thrust points were computed using only the fine grid and second and third-order MUSCL to demonstrate the validity of the calculations across C_t/σ range. At high thrust, it is clear the range of dispersion concerning numerical method and space discretisation. The computational footprint differs for the class of scheme and of course the discretisation order. The attributed cost of each method and the obtained accuracy will determine the overall efficiency of the method. Table 3 shows the computational time in work units per implicit iteration for the simulation of the PSP rotor flow. The work unit is the non-dimensional time required to compute one implicit iteration of the MUSCL2 method at each grid. A similar approach evaluates the cost associated with the number of elements, in this case the MUSCL2 results using the coarsest mesh is taken as reference time and expressed as CPU time. The relative error associated to each simulation is given in percentage of deviation from the FoM experimental measurements (run 156) [46] under the same operating conditions. For a detailed overview of the parallelisation performance of the UCNS3D code, the reader can refer to[50]. All solutions are performed on the Delta, HPC facility, at Cranfield University. The system consists of two intel E5-2620 v4 processors with 16 cores per node and 128GB of shared memory.

The higher cost of WENO scheme is noticeable, as the whole process of computing the reconstruction polynomials arising from several stencils, computing the oscillations indicators and applying a non-linear combination of them is significantly more expensive than a scheme (MUSCL) that uses one reconstruction polynomial per element. In general, at same grid level its

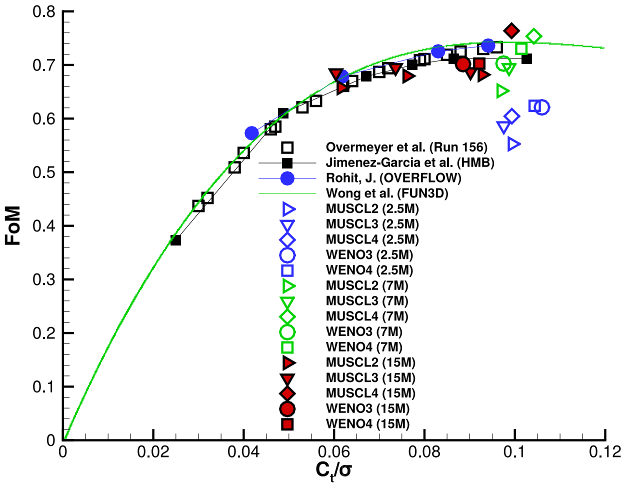

Figure 7: Figure of Merit (FoM) against thrust coefficient C_t/σ (where σ is rotor solidity) for the PSP rotor flow at $M_{tip} = 0.585$. Solutions are shown for all simulations employed both MUSCL and WENO schemes on three grid refinements and three discretisation orders, the CFD data is compared with the experimental data of Overmeyer et al. [46] (opened square symbols) for fixed-transition (Run 156) and published CFD data: HMB [47] (black line), OVERFLOW [48] (blue line) and FUN3D [49] (green line).

Table 3: Computational time and error of the simulated flow over the PSP rotor.

	Scheme	FoM	Work units	Cpu time	Error %
Coarse (2.5M)	MUSCL2	0.55	1.00	1.00	23.35
	MUSCL3	0.59	1.54	1.54	18.68
	MUSCL4	0.60	2.81	2.81	16.17
	WENO3	0.62	3.11	3.11	13.87
	WENO4	0.62	7.43	7.43	13.47
Medium (7.6M)	MUSCL2	0.65	1.00	3.15	9.60
	MUSCL3	0.69	1.58	4.99	3.64
	MUSCL4	0.75	3.13	9.87	4.52
	WENO3	0.70	3.23	10.19	2.55
	WENO4	0.73	7.89	24.85	1.29
Fine (15.2M)	MUSCL2	0.69	1.00	6.94	4.97
	MUSCL3	0.69	1.71	11.86	4.25
	MUSCL4	0.77	3.10	21.47	6.45
	WENO3	0.71	4.14	28.74	2.22
	WENO4	0.71	8.12	56.11	1.03

cost is around three and seven times higher than third- and fourth- order, respectively. This price pays out in terms of accuracy, as WENO results are more accurate. On other hand, MUSCL presents a much cheaper procedure costing up 3 times as the lowest order on the same mesh and delivering a reasonable error level.The computational cost dramatically escalates with the number of elements. Overall, this scalability factor is about the same ratio of elements between the meshes. In this sense, we can compare solutions with the similar precision using different grids. Looking for margin of error lower than 3%, WENO3 on the medium mesh presents the most efficient one since it consumes half of the computational time of the fine mesh using the same scheme. Increasing this margin up to 5%, with a small difference in accuracy MUSCL3 on the medium mesh presents the most cheap scheme using half of the computational time consumed by WENO3.

4.2 S-76

4.2.1 Integrated load with ground effect

The S-76 rotorcraft is one of the main benchmark case for near ground and has been used as validation case for many numerical studies [2]. The experimental study was conducted in a 1/4.71 scaled hovering rotor. The 4-bladed rotor is based on the aerofoil profiles, with a linear twist for 10 deg along the blade's span. The rotor has the radius of 56.1 inches and 3.1 chord length. The rotor performance was measured for several collective pitch angle operating at Mach tip number of 0.55, 0.6 and 0.65 using five tip shapes. The ground effect was considered at three different height-to-radius (z/R) ground positions [41]. This vast experimental dataset consist of many rotor scenarios combinations with isolated main rotor, fuselage and tail rotor. Two flight configurations is assessed here: out-ground and the near-ground ($z/R = 0.75$). For this rotor, the OGE simulation was mainly used for a preliminary comparison for the IGE computations. Then, the IGE simulations, were extended for collective pitch angles of 7 and 11 degrees. To reduce the number of elements the flow is assumed as axisymmetric and then the periodic condition was used. For all simulations, the computational domain has a quarter of a cylindrical shape with radius of 15R and length of 17R. To apply periodicity that the symmetry plane, a cylinder shape hub extending from the whole axial direction with 5% radius rotor R. The ground was treated as free-slip wall to avoid an excessive number of elements at this location. The mesh refinement strategy is conducted in similar manner as previous cases, the meshes are generated based on the number of points on the aerofoil section, blade span and regions of interest. For both cases 50 prismatic layers are placed at boundary layer, with the first element height of 1.0×10^{-6} m. In terms of refinement, the main difference between those meshes are related at the wake. The OGE mesh reached 8.9×10^6 elements, the volumetric local refinement is applied only at the tip blade ($r/R = 1$) near the wake covering up to 0.7 rotor radii downstream the rotor. While on the IGE mesh reached 18.4×10^6 elements, with refinement covering the region between the rotor and the ground.

The computed integrated load for the the pitch angle of 9 degrees are selected as tabulated in Tab. 4 to assess the accuracy within the presence of the ground effect. The comparison is made using three main parameters: trust coefficient (C_t), torque coefficient (C_q), and Figure of Merit (FoM). For the OGE predictions, it can be seen that both C_t and C_q are under-predicted. A small improvement on the torque cofficient as we increase the order. As the FoM is an relation between C_t and C_q, this increment in accuracy with the order can be misread if we look at the FoM solely. For the IGE, the advantage of increasing numerical order is more clear. While the thrust coefficient computed using low-order scheme under-predict the experimental value, the highest order over-predict it just a small bit. The increase in the computed thrust due to the in ground effect is 14.6% while the experiment report approximately 10.4%. Overall, the predicted figure of merit compares well with the experiment for both cases.

In Fig. 8 the predicted blade loading (C_t) and torque coefficient (C_q) for three collective blade pitch angle for IGE simulations are compared with the experimental data. Both coefficient are normalized with the rotor solidity (σ). The computed integrated thrust is slightly over predicted at high collective pitch angle and overshoot for the lowest angle. Overall, for all three collective pitch angles, the computed aerodynamic performance parameters C_t and C_Q agrees well with experimental data.

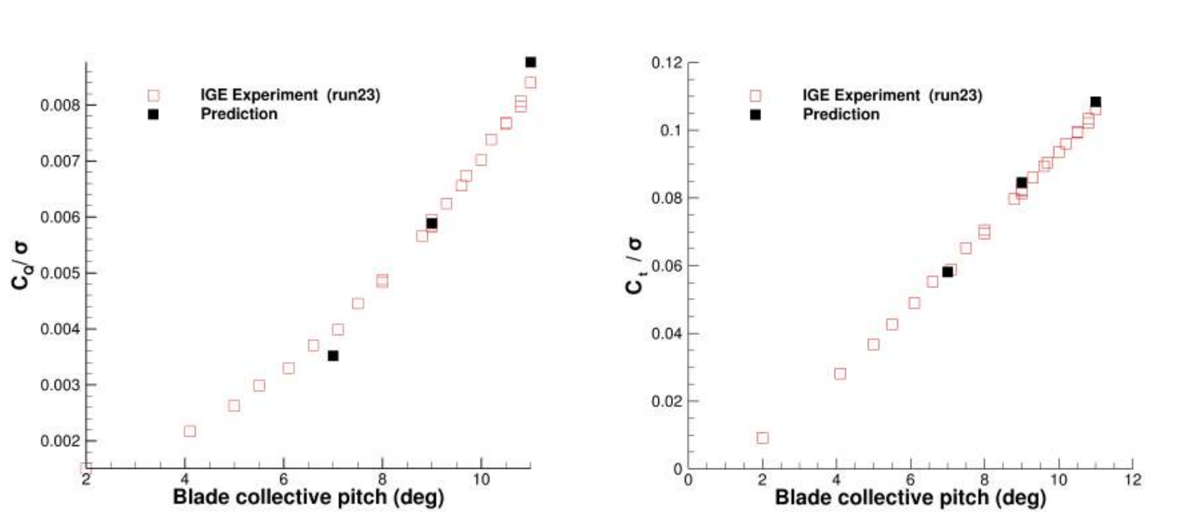

Figure 8: Comparison of predicted and experimental aerodynamic performance parameters for S-76 rotor with ground effect against collective pitch angle: (a) Blade loading coefficient C_t/σ (where σ is rotor solidity) (b) Torque coefficientC_Q/σ .

Table 4: Predicted aerodynamic performance parameters for S76 rotor at collective pitch 9 degrees

	OGE (experimental error)		IGE (experimental error)	
	MUSCL2	MUSCL3	MUSCL2	MUSCL3
C_q/σ	0.00551 (**-3.50%**)	0.00549 (**-3.85%**)	0.00555 (**-4.81%**)	0.00588 (**0.90%**)
C_t/σ	0.073223(**-2.40%**)	0.07403 (**-1.32%**)	0.08596 (**4.64%**)	0.08485 (**3.28%**)
FoM	0.674579 (**-0.08%**)	0.688348 (**1.95%**)	0.85212 (**12.45%**)	0.78834 (**4.03%**)

5 Conclusions

The following major conclusions are derived from the present study:

- pressure coefficients are compared with corresponding experimental data points where high-order solutions better approximate discontinuities and strong gradients.

- In terms of integrated load predictions the most accurate scheme, fourth-order WENO, demonstrates the smallest discrepancies compared with experiment but with the highest registered cost. Assuming a level of accuracy of FoM, the trade-off in terms of cost and accuracy demonstrates that the third-order approach would have the best of both cost and accuracy
- Resolution of the vortex path and wake breakdown are considerably improved with increased scheme order. Using the same mesh the high-order solutions were able to capture in secondary vortex structures.

REFERENCES

[1] Zhou Cheng-Long, Chen Ming, An-An Xu, and Wang Fang. CFD Simulation Methods for Rotor Hovering Based on N-S Equation.

[2] Je Young Hwang and Oh Joon Kwon. Assessment of s-76 rotor hover performance in ground effect using an unstructured mixed mesh method. *Aerospace Science and Technology*, 84:223–236, 2019.

[3] Jianping Hu, Guohua Xu, Yongjie Shi, and Linbo Wu. A numerical simulation investigation of the influence of rotor wake on sediment particles by computational fluid dynamics coupling discrete element method. *Aerospace Science and Technology*, page 106046, 2020.

[4] Tom Stokkermans, Leo Veldhuis, Bambang Soemarwoto, Raphaël Fukari, and Paul Eglin. Breakdown of aerodynamic interactions for the lateral rotors on a compound helicopter. *Aerospace Science and Technology*, page 105845, 2020.

[5] Claudio Pasquali, Jacopo Serafini, Giovanni Bernardini, Joseph Milluzzo, and Massimo Gennaretti. Numerical-experimental correlation of hovering rotor aerodynamics in ground effect. *Aerospace Science and Technology*, page 106079, 2020.

[6] Jennifer N. Abras, Robert Narducci, and Nathan Hariharan. Wake breakdown of high-fidelity simulations of a rotor in hover. In *AIAA Scitech 2019 Forum*. American Institute of Aeronautics and Astronautics Inc, AIAA, 2019.

[7] Stephen L. Wood, James G. Coder, and Nathan S. Hariharan. Fundamental Investigation of Grid Resolution on Wake Fidelity Submitted to the APATC Special Session: Simulation of Rotor in Hover. In *2018 AIAA Aerospace Sciences Meeting*, Reston, Virginia, jan 2018. American Institute of Aeronautics and Astronautics.

[8] UCNS3D CFD code. http://www.ucns3d.com. Accessed: 2022-05-05.

[9] Paulo ASF Silva, Panagiotis Tsoutsanis, and Antonis F Antoniadis. Simple multiple reference frame for high-order solution of hovering rotors with and without ground effect. *Aerospace Science and Technology*, 111:106518, 2021.

[10] Eleuterio F Toro, Michael Spruce, and William Speares. Restoration of the contact surface in the hll-riemann solver. *Shock waves*, 4(1):25–34, 1994.

[11] E.F. Toro. The HLLC Riemann solver. *Journal of Shock Waves*, 29:1065–1082, 2019.

[12] Panagiotis Tsoutsanis. Extended bounds limiter for high-order finite-volume schemes on unstructured meshes. *Journal of Computational Physics*, 362:69–94, 2018.

[13] P. Tsoutsanis, V.A. Titarev, and D. Drikakis. WENO schemes on arbitrary mixed-element unstructured meshes in three space dimensions. *Journal of Computational Physics*, 230(4):1585–1601, 2011.

[14] P. Tsoutsanis, A.F. Antoniadis, and D. Drikakis. WENO schemes on arbitrary unstructured meshes for laminar, transitional and turbulent flows. *Journal of Computational Physics*, 256:254–276, 2014.

[15] P. Tsoutsanis and D. Drikakis. A high-order finite-volume method for atmospheric flows on unstructured grids. *Journal of Coupled Systems and Multiscale Dynamics*, 4:170–186, 2016.

[16] A.F. Antoniadis, P. Tsoutsanis, and D. Drikakis. Numerical accuracy in RANS computations of high-lift multi-element airfoil and aircraft configurations. In *53rd AIAA Aerospace Sciences Meeting*, volume 0317, 2015.

[17] A.F. Antoniadis, P. Tsoutsanis, and D. Drikakis. High-order schemes on mixed-element unstructured grids for aerodynamic flows. In *42nd AIAA Fluid Dynamics Conference and Exhibit*, volume 2833, 2012.

[18] A.F. Antoniadis, P. Tsoutsanis, I. Kokkinakis, Z. Rana, and D. Drikakis. Azure: An advanced CFD software suite based on high-resolution and high-order methods. In *53rd AIAA Aerospace Sciences Meeting*, volume 0813, 2015.

[19] A.F Antoniadis, D. Drikakis, I. W. Kokkinakis, P. Tsoutsanis, and Z. Rana. High-order methods for hypersonic shock wave turbulent boundary layer interaction flow. In *20th AIAA International Space Planes and Hypersonic Systems and Technologies Conference*, volume 3524, 2015.

[20] P. Tsoutsanis, I.W Kokkinakis, L. Konozsy, D. Drikakis, R.J.R. Williams, and D.L. Youngs. Comparison of structured- and unstructured-grid, compressible and incompressible methods using the vortex pairing problem. *Computer Methods in Applied Mechanics and Engineering*, 293:207–231, 2015.

[21] V.A. Titarev, P. Tsoutsanis, and D. Drikakis. WENO schemes for mixed-element unstructured meshes. *Communications in Computational Physics*, 8(3):585–609, 2010.

[22] P. Tsoutsanis and H. Srinivasan. Adaptive mesh refinement techniques for high-order finite-volume WENO schemes. In *ECCOMAS Congress 2016, Crete, Greece*, 2016.

[23] P. Tsoutsanis, N. Simmonds, and A. Gaylard. Implementation of a low-Mach number modification for high-order finite-volume schemes for arbitrary hybrid unstructured meshes. In *ECCOMAS Congress 2016, Crete, Greece*, 2016.

[24] P. Tsoutsanis and D. Drikakis. Addressing the challenges of implementation of high-order finite-volume schemes for atmospheric dynamics on unstructured meshes. In *ECCOMAS Congress 2016, Crete, Greece*, 2016.

[25] P. Tsoutsanis, A.F. Antoniadis, and K.W. Jenkins. Improvement of the computational performance of a parallel unstructured WENO finite volume CFD code for implicit large eddy simulation. *Computers and Fluids*, 173:157–170, 2018.

[26] P.S. Farmakis, P. Tsoutsanis, and X. Nogueira. WENO schemes on unstructured meshes using a relaxed a posteriori MOOD limiting approach. *Computer Methods in Applied Mechanics and Engineering*, 363, 2020.

[27] P. Tsoutsanis. Extended bounds limiter for high-order finite-volume schemes on unstructured meshes. *Journal of Computational Physics*, 362:69–94, 2018.

[28] N. Simmonds, P. Tsoutsanis, A.F. Antoniadis, K.W. Jenkins, and A.. Gaylard. Low-Mach number treatment for finite-volume schemes on unstructured meshes. *Applied Mathematics and Computation*, 336:368–393, 2018.

[29] Francesco Ricci, Paulo ASF Silva, Panagiotis Tsoutsanis, and Antonis F Antoniadis. Hovering rotor solutions by high-order methods on unstructured grids. *Aerospace Science and Technology*, 97:105648, 2020.

[30] P. Tsoutsanis. Stencil selection algorithms for WENO schemes on unstructured meshes. *Journal of Computational Physics: X*, 4, 2019.

[31] P. Tsoutsanis and M. Dumbser. Arbitrary high order central non-oscillatory schemes on mixed-element unstructured meshes. *Computer and Fluids*, 225, 2021.

[32] P. Tsoutsanis, E. M. Adebayo, A. Carriba Merino, A. Perez Arjona, and M. Skote. CWENO finite-volume interface capturing schemes for multicomponent flows using unstructured meshes. *Journal of Scientific Computing*, 89, 2021.

[33] A. F. Antoniadis, P. Tsoutsanis, and D. Drikakis. Assessment of high-order finite volume methods on unstructured meshes for rans solutions of aeronautical configurations. *Computers and Fluids*, 146:86–104, 2017.

[34] V. Maltsev, M. Skote, and P. Tsoutsanis. High-order methods for diffuse-interface models in compressible multi-medium flows: A review. *Physics of Fluids*, 34(2), 2022.

[35] Antonis F Antoniadis, Dimitris Drikakis, Pericles S Farmakis, Lin Fu, Ioannis Kokkinakis, Xesús Nogueira, Paulo ASF Silva, Martin Skote, Vladimir Titarev, and Panagiotis Tsoutsanis. Ucns3d: An open-source high-order finite-volume unstructured cfd solver. *Computer Physics Communications*, page 108453, 2022.

[36] V.P. Kolgan. Application of the minimum-derivative principle in the construction of finite-difference schemes for numerical analysis of discontinuous solutions in gas dynamics. *Transactions of the Central Aerohydrodynamics Institute*, 3(6):68–77, 1972. in Russian.

[37] V.P. Kolgan. Application of the principle of minimizing the derivative to the construction of finite-difference schemes for computing discontinuous solutions of gas dynamics. *J. Comput. Phys.*, 230(7):2384–2390, 2011.

[38] Z J Wang. High-order methods for the Euler and Navier–Stokes equations on unstructured grids. *Progress in Aerospace Sciences*, 43:1–41, 2007.

[39] Francis X Caradonna and Chee Tung. Experimental and analytical studies of a model helicopter rotor in hover. 1981.

[40] A Neal Watkins, Bradley D Leighty, William E Lipford, Kyle Z Goodman, Jim Crafton, and James W Gregory. Measuring Surface Pressures on Rotor Blades Using Pressure-Sensitive Paint.

[41] D. T. Balch and J. Lombardi. Experimental study of main rotor tip geometry and tail rotor interactions in hover. Volume 2: Run log and tabulated data. feb 1985.

[42] J David Kocurek and James L Tangler. A prescribed wake lifting surface hover performance analysis. *Journal of the American Helicopter Society*, 22(1):24–35, 1977.

[43] A.D. Gardner, C.C. Wolf, and M. Raffel. Review of measurement techniques for unsteady helicopter rotor flows. *Progress in Aerospace Sciences*, page 100566, aug 2019.

[44] Kevin W Noonan. Aerodynamic characteristics of two rotorcraft airfoils designed for application to the inboard region of a main rotor blade. 1990.

[45] A Jimenez-Garcia and GN Barakos. Assessment of a high-order muscl method for rotor flows. *International Journal for Numerical Methods in Fluids*, 87(6):292–327, 2018.

[46] Austin D. Overmeyer and Preston B. Martin. Measured Boundary Layer Transition and Rotor Hover Performance at Model Scale. In *55th AIAA Aerospace Sciences Meeting*, Reston, Virginia, jan 2017. American Institute of Aeronautics and Astronautics.

[47] A Jimenez-Garcia and GN Barakos. Numerical simulations on the psp rotor using hmb3. In *2018 AIAA Aerospace Sciences Meeting*, page 0306, 2018.

[48] Rohit Jain. CFD Performance and Turbulence Transition Predictions on an Installed Model-scale Rotor in Hover. In *55th AIAA Aerospace Sciences Meeting*, Reston, Virginia, jan 2017. American Institute of Aeronautics and Astronautics.

[49] Tin-Chee Wong. Application of create tm-av helios in engineering environment: Hover prediction assessment. In *55th AIAA Aerospace Sciences Meeting*, page 1667, 2017.

[50] Panagiotis Tsoutsanis, Antonis F Antoniadis, and Karl W Jenkins. Improvement of the Computational Performance of a Parallel Unstructured WENO Finite Volume CFD code for Implicit Large Eddy Simulation CFD Correlation for Automotive Aerodynamics View project New CFD Techniques for Automotive Aerodynamics View project ART. 2018.